Extreme temperatures on the Greenland ice sheet: a spatial model

Daniel Clarkson[1*], Emma Eastoe[1], and Amber Leeson[2]

[1]School of Mathematical Sciences, Lancaster University, Lancaster, United Kingdom, LA1 4YF
[2]Data Science Institute, Lancaster University, Lancaster, United Kingdom, LA1 4YW

March 12, 2026

[*]Corresponding author. danrclarkson96@gmail.com

Abstract

Whilst surface ice melt from the Greenland ice sheet is one of the largest contributors to sea level rise, our understanding of this phenomenon arises mostly from case studies of specific melt events and the meteorological conditions leading up to them. Although informative, such studies do not facilitate the prediction of future melt nor do they support spatial extrapolation. To address this, we use MODIS satellite surface temperature data to build a statistical spatial extreme value model which can be applied across the entire ice sheet. The model uses a Gaussian mixture model to describe point-wise temperature behaviour, whilst capturing the magnitude, extent, and melt implications of spatial melt events using the full spatial model. By capturing the dependence structure of extreme temperature events, our model enables a better understanding of the stochastic behaviour of extreme melt event characteristics. Through simulation from the model we can also provide predictions of melt probabilities and regional differences in extreme event characteristics. This directly contributes to the Sustainable Development Goals (SDG) - most prominently to SDG 13 (Climate Action) - that aim to improve global sustainability through goals established by the United Nations. Our analysis shows that extreme temperature events are more widespread in the north and east of the ice sheet than in the south, and that the drainage basins of the ice sheet show varying extremal dependence structures.

Keywords— spatial extremes, SDG, Greenland, climate change, spatial melt events

1 Introduction

Rising global sea levels caused by increased ice melt running off ice sheets and glaciers are set to cause devastation in low-lying coastal areas in the near future. The Antarctic and Greenland ice sheets between them provide the largest contribution of melted ice mass to sea level rise (Alley et al., 2005). Their combined influence has increased over the last 30 years (Bamber et al., 2018) and is predicted to contribute up to 25cm to sea levels by 2100 (Golledge et al., 2019). The Greenland ice sheet alone has contributed heavily to the acceleration of sea level rise since the 1970s due to increased mass loss (Frederikse et al., 2020). The mass balance of the ice sheet has been negative since 1998 (van den Broeke et al., 2016; Mouginot et al., 2019) and the ice sheet has been losing ice at an accelerating rate in this recent period (Hanna et al., 2013).

The cause of the increasing melt rates on these ice sheets is climate change, which falls under the remit of the Sustainable Development Goals (SDGs). The SDGs are a set of goals and targets established by the United Nations (UN) in 2015 (Walsh et al., 2022). The goals aim to improve global sustainability and human development by 2030, as well as guiding and shaping global policy on these topics. The SDGs build upon the previous Millennium Development Goals (MDGs) (Evans and Steven, 2012), bringing together economic, environmental and social goals into a single development framework.

Climate change and increasing melt rates are primarily associated with the remit of SDG 13 - take urgent action to combat climate change and its impacts. However, the resulting continued sea level rises will result in the degradation of massive swathes of low-lying coastal land, particularly in Bangladesh, India and China. The consequence of this will impact on the success of multiple other SDGs. As coastal areas become increasingly uninhabitable, the resilience of the poor and vulnerable populations living in these areas will be reduced (in contrast to SDG 1 - No Poverty) and their housing security will decline (in contrast to SDG 11 - Sustainable Cities And Communities). Further, widespread coastal flooding will reduce biodiversity on land (in contrast to SDG 15 - Life On Land), also damaging food security in affected areas (in contrast to SDG 2 - Zero Hunger). The ideal approach would be to halt both climate change and ice melt; however this will not happen fast enough, if it can happen at all. Alongside measures to halt climate change, there must therefore be measures to identify, manage and mitigate the ongoing impacts of climate change. For sea level rise, an improved understanding of how melt is changing can feed predictions of the risk and magnitude of continued sea level rises, which in turn can inform strategic policies to mitigate the adverse effects on coastal regions.

Despite clear evidence that ice melt is increasing, there remains considerable uncertainty on how to forecast this melt and its contributions to sea level rise (Kopp et al., 2017). Estimates of surface mass balance changes are most commonly derived from Regional Climate Models (RCMs) (Fettweis et al., 2017; van Angelen et al., 2013; Burgess et al., 2010), which estimate the total surface mass balance and its constituent components (Lenaerts et al., 2012). RCMs are highly effective at calculating overall totals for melt and surface mass balance but are often less effective at local scales (Medley et al., 2013). For local melt events, observational Ice Surface Temperature (IST) data has been found to better capture the event characteristics (Leeson et al., 2018). However, while observational data has been used to analyse some specific events in

detail (Nghiem et al., 2012), these studies focus on understanding the conditions that led to the events (Bennartz et al., 2013; Hanna et al., 2014) rather than the structure or rarity of the event itself.

The aim of this paper is to address this gap by developing a spatial statistical modelling framework for the frequency, magnitude, and extent of extreme IST events on the Greenland ice sheet. We base our analysis on remote sensing data for the period 2011-2020. Our approach focuses on surface temperatures rather than the binary melt events as understanding how extreme temperature events change over space and time - particularly in regions that have not historically seen ice melt but are likely to do so in the future - is in itself a valuable objective. The insights into melt occurrence, extent, and spatial dependence enhance our ability to predict melt, thereby supporting the climate mitigation and adaptation priorities at the heart of SDG 13. Moreover, the added value of a temperature-based model can be seen by observing that while such a model can be used to predict melt, the reverse is not true.

The most common statistical models for spatial processes are Gaussian processes (Gelfand and Schliep, 2016; Murakami et al., 2020) or Gauss-Markov random fields (Rue and Held, 2005). These models are popular because statistical inference reduces to making inference on a multivariate Gaussian distribution, for which both parameter estimation and prediction are mathematically tractable and relatively straightforward. However, Gaussian processes are rarely suitable for inference on extreme events with a more subtle treatment needed to capture the dependence structure of multivariate, spatial, or temporal extreme values (Schlather and Tawn, 2003). Fortunately, there exist families of multivariate extreme value distributions which are specifically designed to make inference on rare events that occur in the joint tails of a multivariate distribution.

Some excellent and comprehensive reviews of statistical models for extreme events have been conducted in recent years, for example Huser and Wadsworth (2022) and Cooley et al. (2012). We give the briefest of overviews of the two main methods: hierarchical and process-based modelling. In the hierarchical approach, a parametric distribution is used to model the data at each location. The parameters of this distribution are themselves modelled as a smooth spatial process (Sharkey and Winter, 2019; Sang and Gelfand, 2008; Daniel Cooley and Naveau, 2007; Mendes et al., 2010). In contrast, spatial process models seek to model the joint distribution of the response at a finite number of locations on the surface. Examples of processes used in such models include max-stable (S. A. Padoan and Sisson, 2010; Ribatet et al., 2016) and Pareto processes (Palacios-Rodríguez et al., 2020).

In this paper, we use the spatial conditional extremes model (Wadsworth and Tawn, 2022a; Richards et al., 2022; Shooter et al., 2021) which directly models the spatial dependence in the measurements, but is not based on a limiting stochastic process as is the case for max-stable and Pareto processes (Smith, 1990; S. A. Padoan and Sisson, 2010; Ribatet, 2013). This gives it advantages in both flexibility and scalability, providing a strong basis to identify melt patterns and regional climate patterns on the Greenland ice sheet. A second, and perhaps more important, difference between the conditional model and other spatial extremes models, is that the conditional model allows a smooth transition between the two types of extremal dependence. The conditional model smoothly shifts from asymptotic dependence to asymptotic independence with increased separation distance between two locations. This is not the case for max-stable or Pareto processes, which imply asymptotic dependence regardless of sep-

aration distance, and Gaussian processes, which imply asymptotic independence at all separation distances. The flexibility of the conditional model provides a strong basis to identify regional climate extremes on the Greenland ice sheet across varying scales and to improve spatially informed climate risk assessments aligned with SDG 13.

To understand why it is desirable to have a model that can transition across the two types of extremal dependence, consider Figure 1 which shows a map of Greenland with two transects. At each location $\mathbf{s}_j$ on the transects, we transform the data $Y(\mathbf{s}_j)$ to the standard uniform scale $U(\mathbf{s}_j)$ by application of the probability integral transform $U(\mathbf{s}_j) = \tilde{F}(Y(\mathbf{s}_j))$, where $\tilde{F}$ is the empirical cumulative distribution of the measurements at location $\mathbf{s}_j$. For each transect we select an origin location $\mathbf{s}_0$ (grey dots in Figure 1) and obtain the empirical estimate of the metric $\chi(u)$, defined by Coles et al. (1999) to be

$$\chi(u) = \Pr[U(\mathbf{s}_j) > u | U(\mathbf{s}_0) > u], \quad 0 \leq u \leq 1.$$

For u close to 1, this metric is interpreted as the conditional probability that the temperature at location $\mathbf{s}_j$ is high given that the temperature at the base location is high. The edge cases of $\chi(u) = 1$ and $\chi(u) = 0$ correspond to exact dependence and asymptotic independence respectively. For $0 < \chi(u) < 1$, asymptotic dependence increases with $\chi(u)$. Figure 1 shows $\chi(u)$ approaching zero - that is asymptotic independence - as the distance between locations $\mathbf{s}_j$ and $\mathbf{s}_0$ increases. However, it also shows evidence of strong asymptotic dependence at shorter distances. It follows that a model that allows only asymptotic dependence or asymptotic independence will result in under- or over-estimates of the risk of joint extreme events for at least some separation distances. This is crucial for accurate melt risk quantification and assessments of the impacts of climate change.

The remainder of the paper is structured as follows. In Section 2, we describe the IST data set and the methods used to clean the data. In Section 3 we define the marginal Gaussian mixture model and the spatial conditional extremes model. Results of the full spatial extreme value analysis of the Greenland ISTs are presented in Section 4, with a discussion in Section 5.

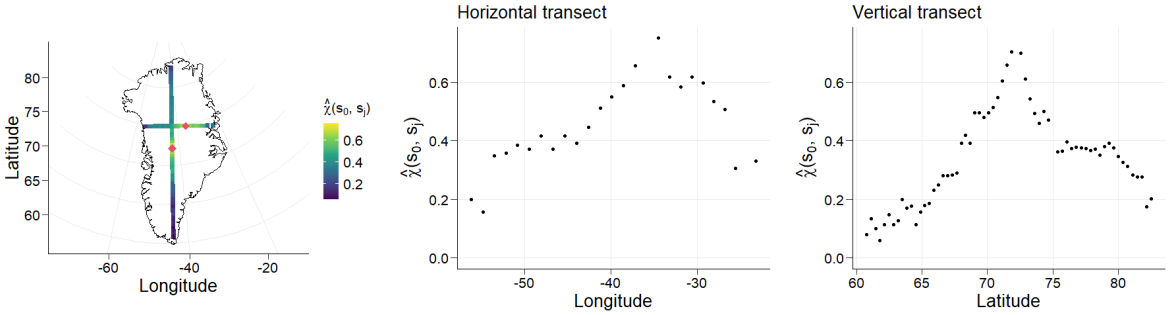

Figure 1: Empirical estimates of χ for $u = 0.975$ across two transects (left), and the estimates of χ plotted against longitude (centre) and latitude (right) for the horizontal and vertical transects respectively. The red diamonds indicate the locations of s_0 for each transect.

2 Data

We use ISTs from the Multilayer Greenland Ice Surface Temperature, Surface Albedo, and Water Vapor product which is derived from Moderate Resolution Imaging Spectroradiometer (MODIS) measurements (Hall and DiGirolamo, 2019). The product has a spatial resolution of 0.78km^2 and has a cloud mask enabling the removal of measurements made when clouds are present in order to avoid measurement noise caused by water vapour in the clouds. Since, at any given time of year, clear days are generally cooler than cloudy days (Koenig and Hall, 2010), the missing data is not entirely missing at random. Further, there is more cloud, and hence more missing data, in winter than in summer (Clarkson et al., 2022). Fortunately, the most extreme temperature events occur almost exclusively in the summer when there are fewer cloudy days and hence less missing data. We use daily data between 2011 and 2020 (inclusive) for all models to balance having an informative sample size against the potential for longer-term climate trends to invalidate modelling assumptions.

2.1 Data cleaning

Exploratory data analysis identified a moderate number of observations that were highly likely to be erroneous. A recent validation of the MODIS data against in-situ measurements from 17 measurement stations on the ice sheet by Zikan et al. (2023), who found a progressive cold bias in MODIS as temperatures decrease, confirms this. Zikan et al. (2023) also found inconsistency between MODIS and in-situ measurements in the above-freezing period, potentially due to errors in the MODIS algorithm, failure of MODIS to correctly identify clouds, or instrumental errors at specific humidities. However, they used only a small number of validation locations, most of which lie close to the coast at relatively low altitudes. Furthermore, above-freezing temperatures are unclipped in MODIS data in contrast to the in-situ measurements, which are truncated at 0°C. Despite this, they still show good agreement.

Because of the agreement between the MODIS data and the non-clipped in-situ observations, and since there is currently no validation across the whole ice sheet, we apply a data-driven approach to filter values that are inconsistent with the expected behaviour for the time of year. For each year-day ($1 \leq d \leq 366$), we take a window comprising all observations within four days of d, treating the year-days as circular such that year-day 1 follows year-day 366. For example, for year-day 10, the observation window consists of observations from year-days $6-14$ inclusive. Year-days for leap years are calculated in the same manner as in other years, as the impact on the calculated values is negligible given the size of the window used, and this avoids either omitting data from leap days or interpolating data for non-leap years. We then calculate the within-window mean μ_d and variance σ_d^2, removing any observations on day d that lie outside of the range $(\mu_d - \lambda\sigma_d^2, \mu_d + \lambda\sigma_d^2)$. A value of $\lambda = 3$ was found to give a suitable balance between excluding outliers and retaining as many observations as possible. Sensitivity to window size was also checked, with 4 days on each side of d found to be large enough to calculate the summary statistics μ_d and σ_d^2, whilst not overly smoothing the data.

2.2 Exploratory Data Analysis

Spatial trends in the ISTs can be seen in Figure 2. A strong seasonal cycle results in a large range in temperatures, as demonstrated by the difference in the 5% and 95% cell-specific quantiles which can be as great as 45°C at a given cell. Melt occurs almost exclusively between May and September (inclusive) and whilst there is variability in temperatures throughout the year, it is insufficient to result in melt temperatures being reached in the winter when mean temperatures are at most −30°C.

The other spatial trends of note are in relation to elevation and latitude/longitude location on the ice sheet. In general, it is warmer at lower elevations and cooler at higher elevations which are mainly in the centre of the ice sheet. The coastal region is also generally warmer, although the rate of change in temperature from the centre to the coast is not consistent across the whole ice sheet. For example, on the west side just below the centre of the ice sheet, both temperature quantiles gradually decrease from the coastline to the centre. In contrast, on the east side, the sharp decline in the temperature quantiles close to the coast becomes a more gradual change closer to the centre of the ice sheet. There are also differences in behaviour in the drainage basins, which split the ice sheet into distinct topological areas that are each drained by a single outlet glacier. These differences will be explored in more detail in Section 4.

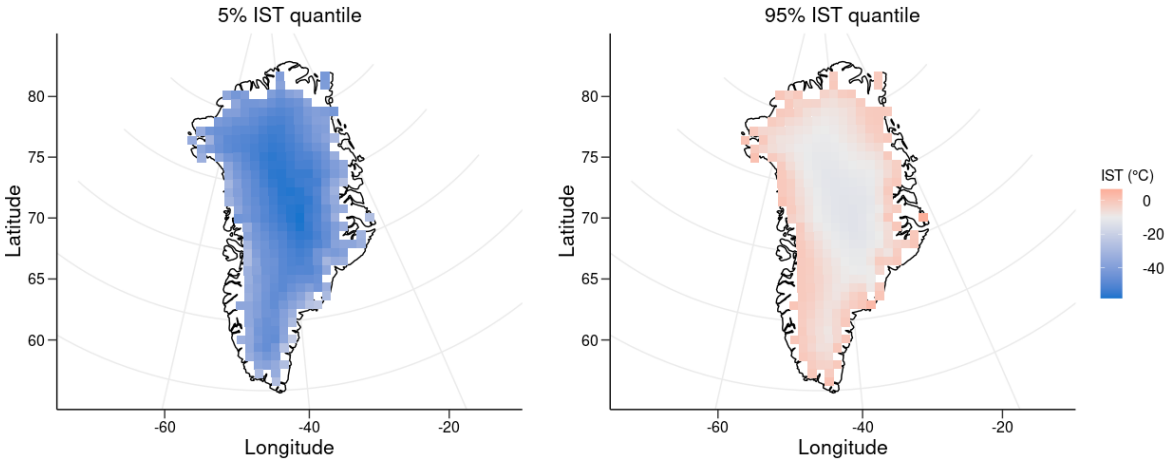

Figure 2: 5% and 95% quantiles of ISTs on the Greenland ice sheet between 2011 and 2020 inclusive. Quantiles are calculated for each individual cell across the entire time period.

3 Methodology

Statistical models for extreme events of spatial processes have a marginal component and a dependence component. The marginal model is usually fitted separately at each location in such a way as to incorporate site-specific behaviour, such as that illustrated

in Section 2.2. The dependence model accounts for any spatial dependence that remains after accounting for the marginal behaviour.

3.1 Marginal model

The objective of the marginal model is to capture the large range of physical characteristics of ISTs across the ice sheet. Because our focus is on the highest ISTs, the routine approach would be to fit a generalised Pareto distribution to the threshold exceedances and model the distribution below the threshold non-parametrically (Davison and Smith, 1990). However, a key characteristic of IST data, referred to as the soft upper limit (Clarkson et al., 2022), makes this approach infeasible. ISTs generally cannot exceed 0°C due to the melting point of ice acting as a physical limit, with additional heat energy contributing to melting rather than increasing the temperature of the ice itself. Consequently, the upper tail of the distribution does not decay as is required for standard extreme value analysis. This challenge is compounded by spatial variability in the marginal distributions since in warmer coastal locations, there are more observations close to 0°C than in the cooler central regions. Consequently, the distributions in cold and warm regions are radically different, requiring a bespoke marginal model in order to maintain a consistent model structure across the ice sheet.

These properties are accounted for using a truncated Gaussian mixture model first defined in our previous study (Clarkson et al., 2023). The model's key assumption is that temperatures indicative of melt have different characteristics and distributional properties than standard ice temperatures. Each component is a truncated Gaussian distribution with truncation points set according to the physical characteristics of the ISTs being modelled. Melt temperatures - modelled by a single mixture component - are lower bounded by -1.65°C as a conservative lower limit of melt temperatures (Hall et al., 2004), and form a single peak in the IST distribution. Ice temperatures are upper bounded by 0°C, modelled by three mixture components as a compromise between parsimony and capturing their multi-modal distribution. ISTs between these limits have an estimated probability of melt to reflect the uncertainty of their true nature.

Full details of the model specification and inference methods can be found in (Clarkson et al., 2023).

3.2 Spatial conditional extremes

The conditional extreme value model introduced by Heffernan and Tawn (2004) and modified by Keef et al. (2013) provides a flexible and efficient way to describe and predict multivariate extreme events. Given a d-dimensional random vector $\mathbf{W} = (W_1, \ldots, W_d)$ with Laplace margins, the model describes the joint stochastic behaviour of the $(d-1)$-dimensional vector $\mathbf{W}_{-i} = (W_1, \ldots, W_{i-1}, W_{i+1}, \ldots, W_d)$ and W_i, conditional on $W_i > t$ as $t \to \infty$. The assumption of Laplace margins is not restrictive since the probability integral transform can be applied to convert data from the original margins to Laplace margins. For the IST data, this transformation uses the Gaussian mixture model described in Section 3.1.

The first step in the model is to define the normalised, or residual, vector $\mathbf{Z}$ with

components

$$Z_j = \frac{W_j - a_{i,j}(w_i)}{b_{i,j}(w_i)},$$

where the normalising functions $a_{i,j}(w_i) = \alpha_{i,j} w_i$ and $b_{i,j}(w_i) = w_i^{\beta_{i,j}}$ have dependence parameters $-1 < \alpha_{i,j} < 1$ and $-\infty < \beta_{i,j} < 1$. The values of the dependence parameters reflect the rate at which w_j increases with w_i. Asymptotic dependence, which occurs when the two variables increase at the same rate, occurs when $\alpha_{i,j} = 1$ and $\beta_{i,j} = 0$. Otherwise, W_i and W_j are asymptotically independent. If either $0 < \alpha_{i,j} < 1$ or $\alpha_{i,j} = 1$ and $\beta_{i,j} > 0$, then the variables are positively dependent, and if $-1 \leq \alpha_{i,j} < 0$ they are negatively dependent. Exact independence occurs when $\alpha_{i,j} = 0$ and $\beta_{i,j} < 0$.

The second step is to define the limiting joint behaviour of $(\mathbf{Z}, W_i)|W_i > v$, as $v \to \infty$, to be

$$\Pr\left[\mathbf{Z} \leq \mathbf{z}, W_i - v > y | W_i > v\right] \to G(\mathbf{z}; \boldsymbol{\theta}_G) \exp\{-y\}, \tag{1}$$

where G is a non-degenerate $(d-1)$-dimensional distribution. Heffernan and Tawn (2004) derive the limit distribution G for a number of common multivariate distributions, but found that there was no unifying class of parametric distributions. For the purposes of parameter estimation, G is therefore routinely taken to be a multivariate Gaussian distribution with unknown mean $\boldsymbol{\mu}$ and diagonal covariance matrix Σ. The conditional extremes model is fitted separately for all d conditioning components, resulting in a total of $4d(d-1)$ parameters.

For spatial data, it is possible to considerably reduce the dimension of the parameter space by directly incorporating spatial structure into the model. This approach has the additional benefit that the resulting model can be used for spatial interpolation. We now briefly describe this extension; further details can be found in Wadsworth and Tawn (2022b).

Let $\{Y(\mathbf{s}) : \mathbf{s} \in S\}$ be a spatial process on the region of interest $\mathcal{S}$ which, in our study, is the Greenland ice sheet. Let $\{W(\mathbf{s}) : \mathbf{s} \in \mathcal{S}\}$ be the same process but on Laplace margins. For each conditioning location $\mathbf{s}_0 \in \mathcal{S}$, define the spatial residual process $\{Z(s) : \mathbf{s} \in \mathcal{S}\}$ as

$$Z(\mathbf{s}) = \frac{W(\mathbf{s}) - a_{\mathbf{s}_0,\mathbf{s}}(W(\mathbf{s}_0))}{b_{\mathbf{s}_0,\mathbf{s}}(W(\mathbf{s}_0))}$$

where $a_{\mathbf{s}_0,\mathbf{s}}(W(\mathbf{s}_0)) \in \mathcal{R}$ and $b_{\mathbf{s}_0,\mathbf{s}}(W(\mathbf{s}_0)) > 0$ are normalising functions for location $\mathbf{s}$. Then the joint behaviour of the residual process and the conditioning variable, as $v \to \infty$, is

$$\left(\{Z(\mathbf{s})\}, W(\mathbf{s}_0) - v\right) | W(\mathbf{s}_0) > v \xrightarrow{d} \left(\left\{Z^0(\mathbf{s})\right\}, E\right), \tag{2}$$

where $Z^0(\mathbf{s})$ is a spatial process for which $Z^0(\mathbf{s}_0) = 0$ almost surely and E is a standard exponential random variable which is independent of $Z^0(\mathbf{s})$. We note that this limit is the infinite-dimensional extension of limit (1). The key assumption for the spatial conditional extremes model is that the limit on the right-hand side of (2) holds exactly provided that the conditioning site is sufficiently large.

The functions $a_{\mathbf{s}_0,\mathbf{s}}$ and $b_{\mathbf{s}_0,\mathbf{s}}$ describe the extremal dependence between location $\mathbf{s}$ and location $\mathbf{s}_0$. Following Wadsworth and Tawn (2022a), we assume that the

strength of dependence decreases smoothly with distance from the conditioning location $\|\mathbf{s} - \mathbf{s}_0\|$. This is achieved through the following parameterisation,

$$\begin{aligned} a_{\mathbf{s}_0,\mathbf{s}}(w) &= w \exp\left\{-\left[\left(\|\mathbf{s} - \mathbf{s}_0\|\right)/\lambda\right]^{\kappa}\right\} \\ b_{\mathbf{s}_0,\mathbf{s}}(w) &= 1 + a_{\mathbf{s}_0,\mathbf{s}}(w)^{\beta}, \end{aligned}$$

where $\lambda > 0$, $\kappa > 0$ and $\beta > 0$. Note that $a_{\mathbf{s}_0,\mathbf{s}_0}(w) = w$, ensuring that $Z(\mathbf{s}_0) = 0$. Furthermore, this parameterisation allows for exact independence at large separation distances, since $a_{\mathbf{s}_0,\mathbf{s}_0}(w) \to 0$ and $b_{\mathbf{s}_0,\mathbf{s}_0}(w) \to 1$ as $\|\mathbf{s}_0 - \mathbf{s}\| \to \infty$. A consequence of this is that, at the greatest separation distances, $Z(\mathbf{s}) \approx W(\mathbf{s})$ and therefore for such locations $Z(\mathbf{s})$ should have the same marginal behaviour as $W(\mathbf{s})$.

The model for the limiting residual process $\{Z^0(\mathbf{s})\}$ is subject to two constraints. First, that $Z^0(\mathbf{s}_0) = 0$, and second that it must have Laplace margins for locations $\mathbf{s}$ that are sufficiently far away from the conditioning location $\mathbf{s}_0$. An intuitive way to build such a process is to start with a standard stationary Gaussian process $\{Z_G(\mathbf{s})\}$ with kernel

$$\rho(d) = \exp\left\{-\left(d/\phi\right)^{\nu}\right\}$$

where $d = \|\mathbf{s} - \mathbf{s}'\|$ is the distance between two locations $\mathbf{s}$ and $\mathbf{s}'$.

A feature of the Gaussian process is that for any set of locations $\mathbf{s}_1, \ldots, \mathbf{s}_m$, the joint distribution of $Z_G(\mathbf{s}_1), \ldots, Z_G(\mathbf{s}_m)$ is a finite-dimensional Gaussian distribution. In particular, the margins are univariate Gaussian.

To incorporate Laplace margins for longer separation distances, the probability integral transform can be used to switch from standard to generalised Gaussian margins. The density for the generalised form of the Gaussian takes the form

$$g_{\mathbf{s}_0,\mathbf{s}}(z) = \frac{\delta_{\mathbf{s}_0,\mathbf{s}}}{2\sigma\Gamma\left(1/\delta_{\mathbf{s}_0,\mathbf{s}}\right)} \exp\left\{-\left|\frac{z-\mu}{\sigma}\right|^{\delta_{\mathbf{s}_0,\mathbf{s}}}\right\}$$

with location μ, scale $\sigma > 0$ and shape $\delta_{\mathbf{s}_0,\mathbf{s}}$ parameters. Restricting $\delta \in [1, 2]$ results in a class of distributions that progresses from the Laplace ($\delta = 1$) to the Gaussian ($\delta = 2$). To enable spatial interpolation, $\delta_{\mathbf{s},\mathbf{s}_0}$ is parameterised to vary with separation distance,

$$\delta_{\mathbf{s}_0,\mathbf{s}} = 1 + \delta_3 \exp\left\{-\left(\frac{||\mathbf{s} - \mathbf{s}_0||}{\delta_1}\right)^{\delta_2}\right\} \tag{3}$$

for shape parameters $\delta_1, \delta_2, \delta_3 > 0$. As the separation distance increases the value of $\delta_{\mathbf{s}_0,\mathbf{s}}$ decreases from 2 to 1, to incorporate the shift from Gaussian to Laplace margins. The constraint that $Z^0(\mathbf{s}_0) = 0$ is straightforward to implement, since the conditional distribution of a multivariate Gaussian distribution is also multivariate Gaussian.

Lastly, we note that the spatial conditional extremes model need only be defined for a single conditioning location since, under the assumption of stationarity, the parameters are the same regardless of conditioning location. Model inference therefore requires estimation of the parameter vector $\boldsymbol{\theta} = (\boldsymbol{\theta}_{\text{dep}}, \boldsymbol{\theta}_{\text{mar}}, \boldsymbol{\theta}_{\text{sp}})$ where $\boldsymbol{\theta}_{\text{dep}} = (\lambda, \kappa, \beta)$ parameterise the dependence functions $a_{\mathbf{s}_0,\mathbf{s}}$ and $b_{\mathbf{s}_0,\mathbf{s}}$, and the spatial process has marginal $\boldsymbol{\theta}_{\text{mar}} = (\mu, \sigma, \delta_1, \delta_2, \delta_3)$ and kernel $\boldsymbol{\theta}_{\text{sp}} = (\phi, \nu)$ parameters.

3.2.1 Inference

Parameter estimation uses a composite likelihood function $L(\boldsymbol{\theta}) = \prod_{k=1}^{d} L_k(\boldsymbol{\theta})$, where each component $L_k(\boldsymbol{\theta})$ is the contribution for a conditioning location. Recall that the limit (2) approximates the spatial process only when the conditioning location is extreme, i.e. when the spatial process $y(\mathbf{s}_0)$ at conditioning location $\mathbf{s}_0$ exceeds a high threshold level v_0. Let $w_{k,t}$ denote the realisation of the spatial surface $W(\mathbf{s}_k)$ at time t. For $k \in \{1, \ldots, d\}$, the contribution to the composite likelihood from location $\mathbf{s}_k$ is then

$$L_k(\boldsymbol{\theta}) = \prod_{t:w_{k,t}>v_k} f_{Z^k}\left(\left[\frac{w_{m,t} - a_{\mathbf{s}_k,\mathbf{s}_m}(w_{k,t};\boldsymbol{\theta}_{\text{dep}})}{b_{\mathbf{s}_k,\mathbf{s}_m}(w_{k,t};\boldsymbol{\theta}_{\text{dep}})}\right]_{m\in\{1,\ldots,d\}\setminus k}; \boldsymbol{\theta}_{\text{mar}}, \boldsymbol{\theta}_{\text{sp}}\right) \cdot \prod_{m\in\{1,\ldots,d\}\setminus k} b_{\mathbf{s}_k,\mathbf{s}_m}(w_{k,t};\boldsymbol{\theta}_{\text{dep}})^{-1}.$$

The function $f_{Z^k}(\mathbf{z})$ is the density for the conditional distribution of $\mathbf{z}$ given that $z_k = 0$. Assuming a Gaussian process with generalised Gaussian margins this takes the form

$$f_{Z^k}(\mathbf{z}) = \phi_{d-1}(\mathbf{z}^0; \Sigma^k) \prod_{m\in\{1,\ldots,d\}/k} \left|\frac{t(z_m)}{z_m}\right|$$

where $\mathbf{z}^0 = (t(z_1), \ldots, t(z_{i-1}), t(z_{i+1}), \ldots, t(z_d))$, and $t(z_m) = \Phi^{-1}(F_{dL}(z_m;\boldsymbol{\theta}_{\text{mar}}))$, where Φ and F_{dL} are the cumulative distribution functions of the standard normal and delta Laplace distributions respectively. The double application of the probability integral transform provides the desired flexibility for the marginal distribution of the residual spatial process. The function ϕ_{d-1} is the density of a $(d-1)$-dimensional multivariate Gaussian random variable with mean $\mathbf{0}$ and correlation matrix $\Sigma^k = (\Sigma_{-k,-k})^{-1}$ where

$$\Sigma_{i,j} = \rho_{i,j} = \exp\{-(||\mathbf{s}_i - \mathbf{s}_j||/\phi)^{\nu}\}.$$

3.3 Uncertainty and bootstrapping

To assess the uncertainty of the model fit and the parameter estimates, we use a stationary bootstrap method (Politis and Romano, 1994) to re-fit the model. We repeat a bootstrap fit of each drainage basin model 100 times, sampling from the set of exceedance days with block lengths generated from a geometric distribution. A mean of 10 is chosen for the geometric distribution as, from exploratory analysis of the data, the expected duration of most climate events is less than 10 days. The resulting set of parameter estimates is then compared to fits of the full non-bootstrapped sample for each drainage basin to assess the uncertainty in the parameter estimates.

3.4 Prediction

It is straightforward to make predictions of the spatial surface $\{Y(\mathbf{s})\}$ given an extreme at a specific conditioning cell s_0. First, the extreme $w^*(\mathbf{s}_0)$ is simulated from a standard

exponential distribution conditional on $w^*(\mathbf{s}_0) > v_0$ where v_0 is the dependence modelling threshold for location $\mathbf{s}_0$. We then independently simulate $z^{0,*}(s)$ from the fitted conditional Gaussian process with delta Laplace margins. From these two quantities, we can simulate $\{W(\mathbf{s}) : \mathbf{s} \in \mathcal{S}\}$ by the reverse transformation

$$\{w^*(\mathbf{s})|W(\mathbf{s}_0) = w^*(\mathbf{s}_0) > v\} = a_{\mathbf{s}_0,\mathbf{s}}(w^*(\mathbf{s}_0)) + b_{\mathbf{s}_0,\mathbf{s}}(w^*(\mathbf{s}_0))z^{0,*}(\mathbf{s}). \tag{4}$$

The simulated process $\{w^*(\mathbf{s})\}$ is transformed back to the original scale $\{y^*(\mathbf{s})\}$ by first applying the probability integral transformation with the Laplace cumulative distribution function and then with the quantile function of the mixture model. Unconditional simulation from the full process is more complex, and we refer the reader to Wadsworth and Tawn (2022a) for full details.

4 Results

We now present our spatial analysis of extreme ISTs in Greenland. For computational reasons, we thin the full data set described in Section 2, retaining only one in every 90 cells in both latitude and longitude directions. As mentioned at the end of Section 2, the ice sheet is split into distinct drainage basins that are pre-defined for all locations on the ice sheet. We categorise all sample cells by the basin in which they fall, excluding cells not assigned to any of these since such cells occur on the coast and do not form part of the continuous spatial surface. We also exclude all cells in drainage basin five, which is located at the southern tip of the ice sheet. This basin is considerably smaller than the other basins. In addition, it has a higher proportion of coastal cells, which tend to have different characteristics to non-coastal cells, and would therefore require a finer sub-sampling scale than the other basins.

4.1 Model Fitting

As discussed in Section 2.2, there are a lot of missing values as the remote sensing equipment fails to make reliable measurements on cloudy days. Not all locations experience missingness simultaneously and whilst an average of 80% of data is available for any given day, in rare instances the number of cells with valid data reaches single digits. Restricting the analysis to only complete cases would result in discarding many surfaces for which measurements are available for the majority of cells. To minimise loss of information, we therefore include days with incomplete observations. This results in 881 days on which an extreme occurs for at least one location, with an average of 90% of cells having an observation on these days.

The marginal models ae fit independently to each cell in the sample using the Expectation-Maximisation (EM) algorithm. Using the Kolmogorov-Smirnov (KS) test as an indication of fit, almost all models are assessed to be a good fit for the data. Six cells were found to have a poorly fitting marginal model from their KS test statistics and were therefore removed from the final sample, leaving 324 cells for use in the spatial models. More details of the marginal model fitting process and results can be found in Appendix 6.1, including boxplots of the bootstrapped parameter estimates in Figure 9.

Figure 3 shows a map of the seven drainage basins that remain after the removal of drainage basin 5, as discussed above. The basins are obtained from the drainage

basin mask contained in the MODIS Greenland product (Hall and DiGirolamo, 2019). The spatial conditional extreme value model is fit separately to each of the seven drainage basins in our sample. Point estimates of the model parameters, shown in Table 1, are obtained by taking the median of the bootstrapped sampling distributions. The full bootstrap sampling distributions can be seen in Appendix 6.2. Using the point estimates, we can also estimate the dependence functions a and b as functions of distance from the conditioning site.

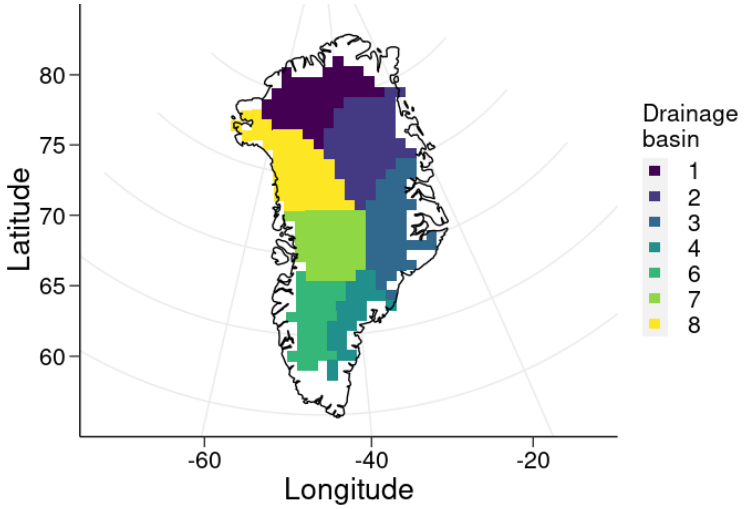

Figure 3: Sample of points for spatial conditional extremes model fits in each Drainage basin.

Table 1: Parameter estimates for the spatial conditional extremes model fitted to seven of the Greenland drainage basins.

Basin	μ	σ	ϕ	ν	δ_1	δ_2	δ_3	λ	κ	β
1	-0.12	0.48	491.34	0.55	239.80	0.24	1.29	3466.37	0.63	0.77
2	0.08	0.56	805.93	0.56	44.99	0.21	2.05	1837.73	0.48	0.77
3	-0.53	0.66	4668.97	0.31	230.86	0.25	1.60	1459.41	1.03	0.66
4	-0.56	0.76	5014.91	0.36	89.08	0.27	1.35	861.35	0.56	0.76
6	1.22	0.98	5021.81	0.35	85.71	0.31	0.42	19.23	0.23	0.87
7	0.01	0.64	424.75	0.59	82.99	0.14	2.03	1784.54	0.49	0.60
8	0.16	0.67	667.20	0.50	134.22	0.28	1.82	1045.81	0.56	0.66

Figure 4 shows that the dependence functions for basins 6, 4, 8, 2, and 7 (in order from fastest to slowest rate of decrease) decrease faster than those for basins 1 and 3, indicating that cells in these basins have weaker dependence at greater distances.

Basins 4, 8, 2, and 7 each have estimated a functions that decrease steadily over the range of distances observed, reaching minimum values close to 0.4 (basins 4 and 8), 0.5 (basin 2), and 0.6 (basin 7). In contrast, the estimated b functions of all of these basins remain above 1.5. This indicates that at the maximum distances observed, the dependence in any basin does not reach asymptotic independence, even in the case of

basin 6. Basins 1 and 3 display higher values in their dependence functions. Basin 3 has the highest dependence estimates over short distances, although basin 1 decreases at a slower rate and therefore has a higher estimate for a and b at the extent of its range.

Basin 6, located in the south west, displays particularly distinctive behaviour, with dependence function estimates that fall very rapidly to a level below those of the other basins. This arises from the very small estimated value for λ for this basin, implying that there is only very localised extremal dependence between cells in this basin. Whilst basin 6 does not have any obvious physical or geographical features that distinguish it in terms of shape, coastal properties, or size, note that - as distance increases - the two southern basins (4 and 6) see the fastest decrease in dependence, whereas basin 1, the most northerly basin, sees the slowest decrease. Furthermore, in general basins on the east side of the ice sheet have higher dependence than those on the west of the ice sheet. Combining these points suggests that events become more localised for basins further to the south and west of the ice sheet.

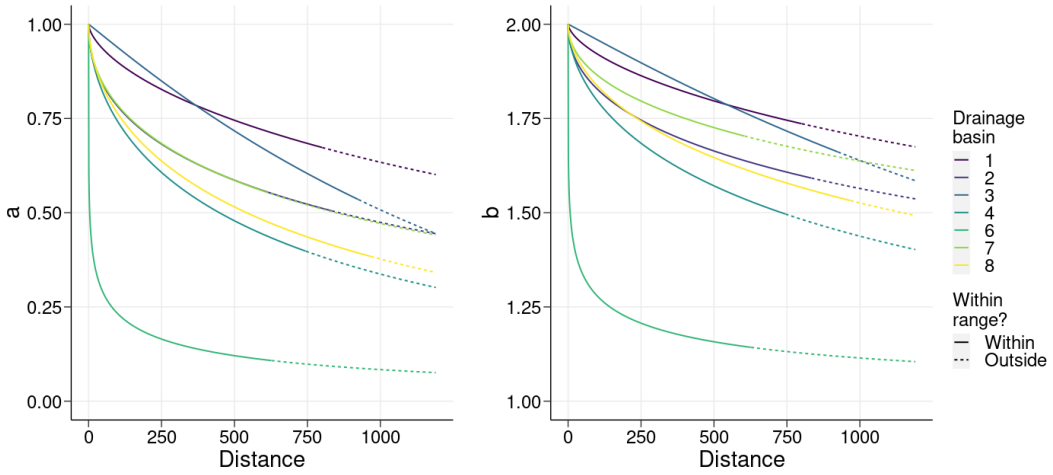

Figure 4: Dependence functions $a_{\mathbf{s}_0,\mathbf{s}}$ and $b_{\mathbf{s}_0,\mathbf{s}}$ estimated from the fitted parameters for each drainage basin. Distance is measured from the conditioning cell, $||\mathbf{s}_0 - \mathbf{s}||$. Dotted lines indicate that estimates are taken outside the maximum sample distance within each drainage basin.

The estimates for $\delta_{\mathbf{s}_0,\mathbf{s}}$ vary less between the drainage basins. The general trend seen across all basins (Figure 5) is that, as a function of distance from the conditioning cell, the estimated $\delta_{\mathbf{s}_0,\mathbf{s}}$ quickly decreases below 1.5 for distances less than 100km, before stabilising at values between 1.2 and 1.35. This re-affirms the inference from the dependence function estimates that temperatures are asymptotically dependent to some degree over all observed distances in the drainage basins. The estimates also demonstrate that $\delta_{\mathbf{s}_0,\mathbf{s}}$ quickly changes from its value at $\mathbf{s}_0$ to other cells in the sample. Estimates of $\delta_{\mathbf{s}_0,\mathbf{s}}$ start at values greater than 1.5 for all basins then quickly decay below this, even for short distances. This suggests that the marginal distributions of exceedances are distinctly different once the model moves away from $\mathbf{s}_0$, and that the distributions do not reach a Laplace distribution for which $\delta_{\mathbf{s}_0,\mathbf{s}} = 1$.

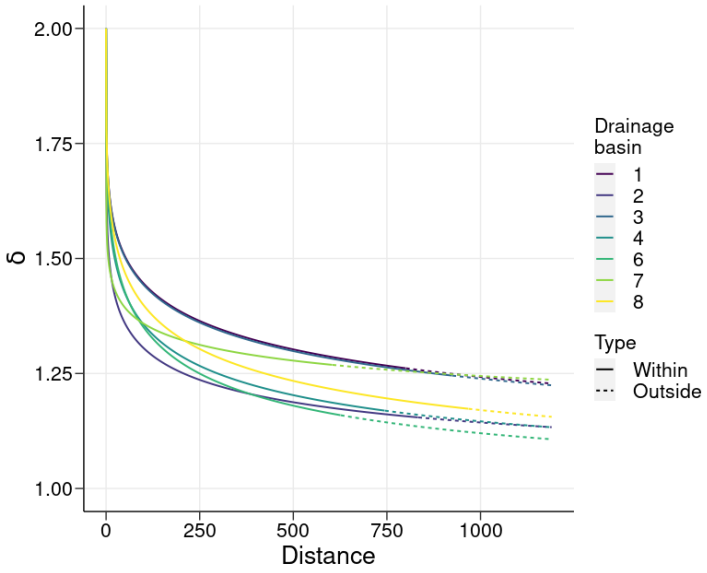

Figure 5: Estimates for δ from the fitted parameters for each drainage basin. Distance is measured from the conditioning cell, $||\mathbf{s}_0 - \mathbf{s}||$. Dotted lines indicate that estimates are taken outside the maximum sample distance within each drainage basin.

4.2 Predictions

To better understand the spatial extent of IST extreme events, we explore some surfaces simulated from the fitted models. Since thresholds are defined using a within-cell quantile, we can assume that all cells in a given basin are equally likely to produce an exceedance. Taking each cell in turn as the conditioning location, we simulate a total of 50 events per conditioning cell. For each cell $\mathbf{s}_k$, this set of simulated events is used to estimate the *co-occurrence probability*, that is the probability that an exceedance occurs in at least one other cell, given that an exceedance has occurred at $\mathbf{s}_k$.

The estimated co-occurrence probabilities, shown in Figure 6a, present a more distinct spatial trend than the dependence function estimates. Specifically, the average of the cell-exceedance rates for the two southern basins (4 and 6) is much lower than for the rest of the ice sheet - on average, events contain only 38.3% of the cells in the basin. In contrast, for the northern (1, 2, and 8) and central-western (7) basins, the mean lies around 62%. There is also a slight trend for smaller co-exceedance proportions closer to the coast, although this is less pronounced than the north-south discrepancy.

Events in the central-eastern basin (3) are more widespread than in the southern basins but more localised than in the northern and central-western basins, with an average co-occurrence rate of 51%. This conclusion seemingly contradicts the previous observation from Figure 4 that the dependence on the eastern side is stronger than on the west. This discrepancy may be explained by noting that the central-western basin has lower maximum between-cell distances than the central-eastern one. Hence, although the dependence decays faster with increasing distance in the west than in the east, the expected dependence at the maximum between-cell distance within the central-western basin is higher than the equivalent value for the central-eastern basin, simply because the maximum between-cell distance is much greater in the latter basin

than in the former. Furthermore, the mean estimate for basin 3 is much lower (around -0.5) than those of the northern basins (around 0). This means that, despite similar dependency between ISTs in these basins, the initial drop in IST between s_0 and the closest non-conditioning sites is enough to push more cells below their thresholds. Therefore, fewer cells share extremes with basin 3 than is the case for the other northern basins.

The event sizes may also indicate that basins with different elevation profiles show differing dependence characteristics. The two southern basins that show distinct extreme event size properties have overall lower elevation profiles (in terms of mean and maximum elevation) than the central basins where the peak of the ice sheet is located. Elevation also distinguishes the two central basins, as the central-eastern basin has the highest consistent elevation values out of all basins studied. Even after marginal characteristics have been accounted for, the difference in elevation profile between basins may contribute to the difference in event sizes, as well as the distinction between the extremal characteristics of the two southern basins and all other basins.

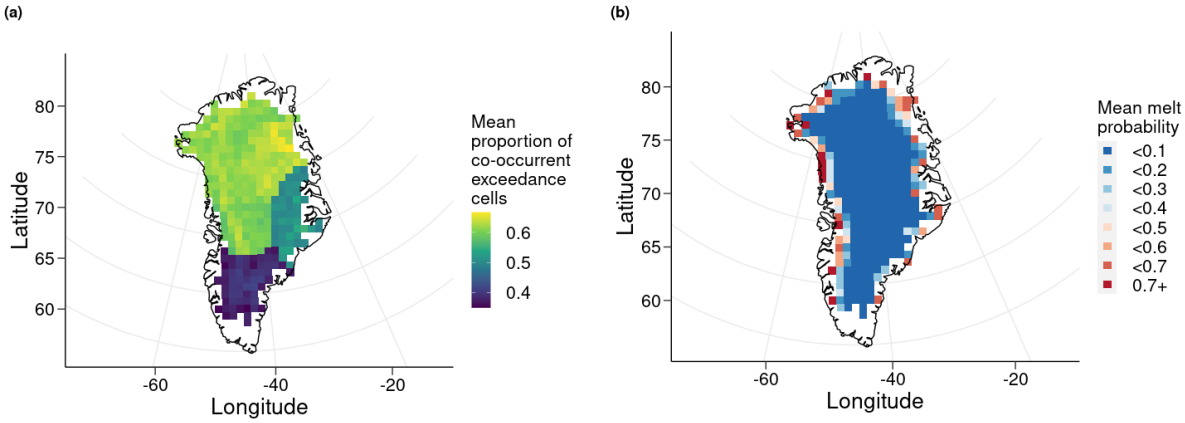

Figure 6: The mean number of co-exceedances in each cell from conditional simulations of the fitted basin models (a), and mean melt probabilities of each cell from spatial extreme events. Using simulations from each basin, estimated melt probabilities of each simulation are calculated using the marginal Gaussian mixture model to estimate melt (b).

There is substantial variance in the size of the model-based extreme event simulations. For each simulated event, we define extent as the proportion of cells in the basin that experience a threshold exceedance during the event. A boxplot of the resulting extent estimates is shown in Figure 7. All basins, including those in the south, have simulations close or equal to both the minimum (1 cell) and the maximum (all cells) possible extent. Most of the basins are estimated to have the potential for large spatial extreme events, with only basins 4 and 6 in the south having generally more localised events that generally cover less than 60% of the basin. The median event size similarly reflects this, as the southern basins show the same trend for event size as the mean of the event co-exceedance proportions. However, the distribution of the event extents for basin 3 are more similar to those for basins 4 and 6 than previously seen in the co-exceedance proportions, suggesting that basin 3 may have more similar behaviour to the south than the rest of the ice sheet.

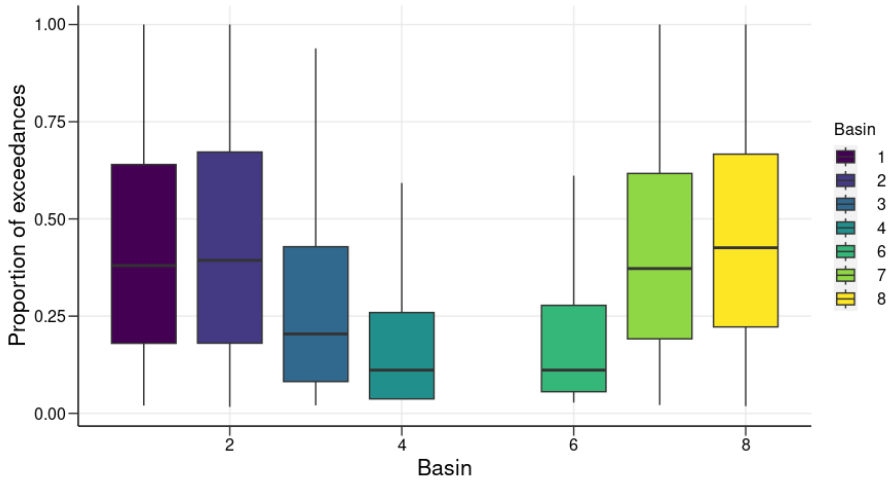

Figure 7: Distribution of the extent of all simulated extreme events by basin.

Lastly, we show how the spatial model for IST can be used to predict the pointwise melt probabilities (Clarkson et al., 2022) across the ice sheet. For a given cell, the melt probability is estimated for each simulated event that involves that cell, with the mean of these melt probabilities used as the point estimate for the cell. Figure 6b shows a map of the estimated melt probabilities for all cells in the basin samples. The melt patterns from the extreme events broadly match those of the independent marginal models. However, because the simulations are based only on extreme events rather than all temperatures, the estimated melt probability is higher for all cells than the overall trends. The trends in mean melt probability are more strongly influenced by the geography of the entire ice sheet rather than that of specific drainage basins. Cells closer to the coast have a higher mean probability from the simulations, with a maximum of 0.92 for a cell in basin 8. This does not extend far into the centre of the ice sheet though, and overall around 71.9% of all cells have a mean melt probability of < 0.1 even when conditioning on only extreme events.

5 Discussion

The spatial conditional extremes model can be used successfully on data that typically would not be considered for extreme value analysis via the use of a suitable, well-defined marginal model. Despite melt being considered an extreme quantity, MODIS IST data does not have a tail or distributional properties that function within an extreme value modelling framework. However, by combining the spatial extremes model with a Gaussian mixture model, we have modelled and simulated spatial melt events to gain more insight into their structure than is possible from observations alone. In this case, our marginal model is not a model associated with extreme value analysis and is instead defined much more specifically using domain-specific knowledge of the variable being modelled. Finding a suitable marginal form for the data provides a solid foundation of understanding, without which it would not be possible to analyse these extreme events spatially.

From the fitted models and the simulations, we observe differing structures in spatial extreme events across the ice sheet. While there is a higher probability of melting further south on the ice sheet, events in the south and west appear more localised than those in the north and east. This suggests that higher temperatures in the north and east that cause melt could lead to relatively larger melt events than in the south and west, even if they are less likely to occur from the observed data. This demonstrates the potential risk posed by an increase in temperatures on the ice sheet from further climate change, as while these extreme events are based on quantiles rather than the melt threshold, higher overall temperatures will result in these extreme events being pushed further towards and over the melt threshold.

The scale of the ice sheet and the capacity of the spatial conditional extremes model mean that there is some uncertainty as to how the trends in extremal dependence would translate to much smaller distances. There is far more data from MODIS IST (approximately 4,000,000 cells of ice sheet data) than can reasonably be processed in a spatial extremes model. We choose to focus on the larger-scale events that affect large proportions of the ice sheet, but analysis of smaller-scale events could provide different types of insight. Analysis of small-scale events on the coasts compared to the centre of the ice sheet, events on particular surface conditions, or at locations exposed to certain atmospheric conditions would all present a different lens into spatial temperature extremes on the ice sheet that can be obtained from an analysis of the entire ice sheet at once. Furthermore, a more detailed examination of the impact of elevation and other physical characteristics of the ice sheets on extreme temperatures could help to further distinguish and characterise how these events differ across the ice sheet.

We also note that any inferences apply to clear days only, and acknowledge that the marginal model fits may be slightly more heavily weighted towards higher temperatures than they would be if all of the data were available. Accurately replacing the missing data would provide predictions valid for any weather conditions, but this would also require data related to weather conditions on the ice sheet and a more well-defined relationship between temperatures in different sets of climate conditions. Furthermore, the missing data presents a challenge in applying the spatial model to the data since almost all days in the sample have some degree of missing data. Although we account for this by scaling Z^0 to a dimension matching the amount of available data, more information about the conditions in the missing regions would be needed to further develop these model adaptations.

Further work in examining the frequency and impact of extreme events is crucial in understanding the future effects of climate change on the ice sheets for SDG 13. Spatial extreme models provide a natural perspective on all spatial extreme temperature events of a chosen magnitude, but statistical analysis of particularly extreme temperature events that are only seen once or twice in the data would also be of significant value. In some cases, this type of analysis would lend itself more to a compound extremes type of model, whereby multiple extreme factors (air pressure, temperature etc.) contribute to an event larger than the sum of their individual impacts. This would require collaboration between glaciologists and statisticians to both accurately represent and model the relevant glaciological conditions, in addition to developing compound extreme value models that consider the impact of jointly extreme events. These models are key to understanding the complexity of the climate system and the

interactions between climate variables in relation to melt. In a similar manner to the events described in this study, once a statistical form has been identified for compound events, changes in the inputs to the system such as those resulting from climate change can be used to examine how these events may change in the future under different climate scenarios.

Acknowledgements

DC, EE and AL were supported by the EPSRC-funded Data Science of the Natural Environment project (EP/R01860X/1).

Disclosure statement

The authors report there are no competing interests to declare.

Data availability

The MODIS data that supports these findings is available online (`https://doi.org/10.5067/7THUWT9NMPDK`) from the Multilayer Greenland Ice Surface Temperature, Surface Albedo, and Water Vapor from MODIS, Version 1 dataset (Hall and DiGirolamo, 2019).

References

Alley, R. B., Clark, P. U., Huybrechts, P., and Joughin, I. (2005). Ice-sheet and sea-level changes. *Science*, 310(5747):456–460.

Bamber, J. L., Westaway, R. M., Marzeion, B., and Wouters, B. (2018). The land ice contribution to sea level during the satellite era. *Environmental Research Letters*, 13(6):063008.

Bennartz, R., Shupe, M., Turner, D., Walden, V., Steffen, K., Cox, C., Kulie, M., Miller, N., and Pettersen, C. (2013). July 2012 Greenland melt extent enhanced by low-level liquid clouds. *Nature*, 496:83–6.

Burgess, E. W., Forster, R. R., Box, J. E., Mosley-Thompson, E., Bromwich, D. H., Bales, R. C., and Smith, L. C. (2010). A spatially calibrated model of annual accumulation rate on the greenland ice sheet (1958–2007). *Journal of Geophysical Research: Earth Surface*, 115(F2).

Clarkson, D., Eastoe, E., and Leeson, A. (2022). Melt probabilities and surface temperature trends on the Greenland ice sheet using a Gaussian mixture model. *The Cryosphere*, 16(5):1597–1607.

Clarkson, D., Eastoe, E., and Leeson, A. (2023). The importance of context in extreme value analysis with application to extreme temperatures in the US and Greenland. *Journal of the Royal Statistical Society Series C: Applied Statistics*, 72(4):829–843.

Coles, S., Heffernan, J., and Tawn, J. (1999). Dependence measures for extreme value analyses. *Extremes*, 2:339–365.

Cooley, D., Cisewski, J., Erhardt, R. J., Jeon, S., Mannshardt, E., Omolo, B. O., and Sun, Y. (2012). A survey of spatial extremes: Measuring spatial dependence and modeling spatial effects. *REVSTAT-Statistical Journal*, 10(1):135–165.

Daniel Cooley, D. N. and Naveau, P. (2007). Bayesian spatial modeling of extreme precipitation return levels. *Journal of the American Statistical Association*, 102(479):824–840.

Davison, A. C. and Smith, R. L. (1990). Models for Exceedances over High Thresholds. *Journal of the Royal Statistical Society. Series B (Methodological)*, 52(3):393–442.

Evans, A. and Steven, D. (2012). *Sustainable Development Goals: A Useful Outcome from Rio+ 20?* Center on International Cooperation.

Fettweis, X., Box, J. E., Agosta, C., Amory, C., Kittel, C., Lang, C., van As, D., Machguth, H., and Gallée, H. (2017). Reconstructions of the 1900–2015 Greenland ice sheet surface mass balance using the regional climate mar model. *The Cryosphere*, 11(2):1015–1033.

Frederikse, T., Landerer, F., Caron, L., Adhikari, S., Parkes, D., Humphrey, V., Dangendorf, S., Hogarth, P., Zanna, L., Cheng, L., and Wu, Y.-H. (2020). The causes of sea-level rise since 1900. *Nature*, 584:393–397.

Gelfand, A. E. and Schliep, E. M. (2016). Spatial statistics and Gaussian processes: A beautiful marriage. *Spatial Statistics*, 18:86–104. Spatial Statistics Avignon: Emerging Patterns.

Golledge, N. R., Keller, E. D., Gomez, N., Naughten, K. A., Bernales, J., Trusel, L. D., and Edwards, T. L. (2019). Global environmental consequences of twenty-first-century ice-sheet melt. *Nature*, 566(7742):65—72.

Hall, D., Key, J., Casey, K., Riggs, G., and Cavalieri, D. (2004). Sea ice surface temperature product from modis. *IEEE Transactions on Geoscience and Remote Sensing*, 42(5):1076–1087.

Hall, D. K. and DiGirolamo, N. (2019). Multilayer greenland ice surface temperature, surface albedo, and water vapor from MODIS, Version 1.

Hanna, E., Fettweis, X., Mernild, S. H., Cappelen, J., Ribergaard, M. H., Shuman, C. A., Steffen, K., Wood, L., and Mote, T. L. (2014). Atmospheric and oceanic climate forcing of the exceptional Greenland ice sheet surface melt in summer 2012. *International Journal of Climatology*, 34(4):1022–1037.

Hanna, E., Navarro, F., Pattyn, F., Domingues, C., Fettweis, X., Ivins, E., Nicholls, R., Ritz, C., Smith, B., Tulaczyk, S., Whitehouse, P., and Zwally, H. (2013). Ice-sheet mass balance and climate change. *Nature*, 498:51–9.

Heffernan, J. E. and Tawn, J. A. (2004). A conditional approach for multivariate extreme values (with discussion). *Journal of the Royal Statistical Society Series B: Statistical Methodology*, 66(3):497–546.

Huser, R. and Wadsworth, J. L. (2022). Advances in statistical modeling of spatial extremes. *WIREs Computational Statistics*, 14(1):e1537.

Keef, C., Papastathopoulos, I., and Tawn, J. A. (2013). Estimation of the conditional distribution of a multivariate variable given that one of its components is large: Additional constraints for the Heffernan and Tawn model. *Journal of Multivariate Analysis*, 115:396–404.

Koenig, L. S. and Hall, D. K. (2010). Comparison of satellite, thermochron and air temperatures at Summit, Greenland, during the winter of 2008/09. *Journal of Glaciology*, 56(198):735–741.

Kopp, R. E., DeConto, R. M., Bader, D. A., Hay, C. C., Horton, R. M., Kulp, S., Oppenheimer, M., Pollard, D., and Strauss, B. H. (2017). Evolving understanding of Antarctic ice-sheet physics and ambiguity in probabilistic sea-level projections. *Earth's Future*, 5(12):1217–1233.

Leeson, A. A., Eastoe, E., and Fettweis, X. (2018). Extreme temperature events on Greenland in observations and the mar regional climate model. *The Cryosphere*, 12(3):1091–1102.

Lenaerts, J. T. M., van den Broeke, M. R., van Angelen, J. H., van Meijgaard, E., and Déry, S. J. (2012). Drifting snow climate of the greenland ice sheet: a study with a regional climate model. *The Cryosphere*, 6(4):891–899.

Medley, B., Joughin, I., Das, S. B., Steig, E. J., Conway, H., Gogineni, S., Criscitiello, A. S., McConnell, J. R., Smith, B. E., van den Broeke, M. R., Lenaerts, J. T. M., Bromwich, D. H., and Nicolas, J. P. (2013). Airborne-radar and ice-core observations of annual snow accumulation over Thwaites Glacier, West Antarctica confirm the spatiotemporal variability of global and regional atmospheric models. *Geophysical Research Letters*, 40(14):3649–3654.

Mendes, J., Bermudez, P., Pereira, J., Turkman, K., and Vasconcelos, M. (2010). Spatial extremes of wildfire sizes: Bayesian hierarchical models for extremes. *Environmental and Ecological Statistics*, 17:1–28.

Mouginot, J., Rignot, E., Bjørk, A., Van den Broeke, M., Millan, R., Morlighem, M., Noël, B., Scheuchl, B., and Wood, M. (2019). Forty-six years of Greenland ice sheet mass balance from 1972 to 2018. *Proceedings of the National Academy of Sciences*, 116.

Murakami, D., Yamagata, Y., and Hirano, T. (2020). Chapter four - geostatistics and Gaussian process models. In Yamagata, Y. and Seya, H., editors, *Spatial Analysis Using Big Data*, pages 57–112. Academic Press.

Nghiem, S. V., Hall, D. K., Mote, T. L., Tedesco, M., Albert, M. R., Keegan, K., Shuman, C. A., DiGirolamo, N. E., and Neumann, G. (2012). The extreme melt across the Greenland ice sheet in 2012. *Geophysical Research Letters*, 39(20).

Palacios-Rodríguez, F., Toulemonde, G., Carreau, J., and Opitz, T. (2020). Generalized Pareto processes for simulating space-time extreme events: an application to precipitation reanalyses. *Stochastic environmental research and risk assessment*, 34:2033–2052.

Politis, D. N. and Romano, J. P. (1994). The stationary bootstrap. *Journal of the American Statistical Association*, 89(428):1303–1313.

Ribatet, M. (2013). Spatial extremes: Max-stable processes at work. *Journal de la société française de statistique*, 154(2):156–177.

Ribatet, M., Dombry, C., and Oesting, M. (2016). Spatial extremes and max-stable processes. *Extreme value modeling and risk analysis: methods and applications*, pages 179–194.

Richards, J., Tawn, J. A., and Brown, S. (2022). Modelling extremes of spatial aggregates of precipitation using conditional methods. *The Annals of Applied Statistics*, 16(4):2693 – 2713.

Rue, H. and Held, L. (2005). *Gaussian Markov random fields: theory and applications*. Chapman and Hall/CRC.

S. A. Padoan, M. R. and Sisson, S. A. (2010). Likelihood-based inference for max-stable processes. *Journal of the American Statistical Association*, 105(489):263–277.

Sang, H. and Gelfand, A. (2008). Hierarchical modeling for extreme values observed over space and time. *Environmental and Ecological Statistics*, 16:407–426.

Schlather, M. and Tawn, J. A. (2003). A dependence measure for multivariate and spatial extreme values: Properties and inference. *Biometrika*, 90(1):139–156.

Sharkey, P. and Winter, H. C. (2019). A Bayesian spatial hierarchical model for extreme precipitation in great britain. *Environmetrics*, 30(1):e2529. e2529 env.2529.

Shooter, R., Tawn, J., Ross, E., and Jonathan, P. (2021). Basin-wide spatial conditional extremes for severe ocean storms. *Extremes*, 24(2):241–265.

Smith, R. L. (1990). Max-stable processes and spatial extremes. *Unpublished manuscript*, 205:1–32.

van Angelen, J., Van den Broeke, M., Wouters, B., and Lenaerts, J. (2013). Contemporary (1960–2012) evolution of the climate and surface mass balance of the Greenland ice sheet. *Surv Geophys*, 35:1–20.

van den Broeke, M. R., Enderlin, E. M., Howat, I. M., Kuipers Munneke, P., Noël, B. P. Y., van de Berg, W. J., van Meijgaard, E., and Wouters, B. (2016). On the recent contribution of the Greenland ice sheet to sea level change. *The Cryosphere*, 10(5):1933–1946.

Wadsworth, J. and Tawn, J. (2022a). Higher-dimensional spatial extremes via single-site conditioning. *Spatial Statistics*, 51:100677.

Wadsworth, J. L. and Tawn, J. (2022b). Higher-dimensional spatial extremes via single-site conditioning. *Spatial Statistics*, 51:100677.

Walsh, P. P., Banerjee, A., and Murphy, E. (2022). The UN 2030 agenda for sustainable development. In *Partnerships and the sustainable development goals*, pages 1–12. Springer.

Zikan, K. H., Adolph, A. C., Brown, W. P., and Fausto, R. S. (2023). Comparison of modis surface temperatures to in situ measurements on the Greenland ice sheet from 2014 to 2017. *Journal of Glaciology*, 69(273):129–140.

6 Appendix

6.1 Marginal model fits

For each of the 330 cells in the cleaned and thinned data set, we first obtain separate cell fits of the Gaussian mixture distribution. These will be the marginal models for the spatial extremes model, but they also provide an initial insight into both the quantity of melt across the ice sheet and any spatial trends in this melt. The models are fitted independently to the data for each cell, using the EM algorithm with 6000 iterations. Model fit is assessed using the KS test. The KS test statistic is defined as:

$$D_n = \sup_x |F_n(x) - F(x)| \tag{5}$$

where $F_n(x)$ is the empirical distribution function for n ordered observations, $F(x)$ is the fitted cumulative distribution function, and $\sup_x$ is the supremum of the set of distances between the two functions. Using a significance level of 0.05, we find that at 98.18% (324 of the 330) cells, the null hypothesis that the observations were drawn from the fitted mixture model distributions is not rejected, indicating that the marginal models fit well for the majority of cells in our sample.

Figure 8 displays the p-values for the KS test. From this plot, it is clear that almost all of the poorly fitting mixture models correspond to coastal cells on the edge of the ice sheet. This is not entirely surprising since ISTs on the coasts of the ice sheet are known to behave differently from those in more central areas. Ambiguity in the surface conditions and uncertainty over whether they remain ice for the entire year can cause some coastal ISTs to far exceed 0°C. Consequently, we remove the six cells with a significant KS score from our sample to ensure that there is a sufficiently good marginal fit at all sampled cells, leaving a final sample of 324 cells.

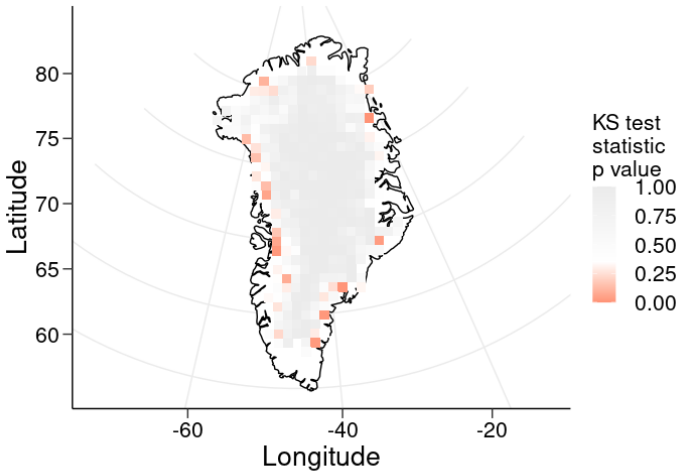

Figure 8: KS test statistic p-values as defined in Section 6.1 evaluated for every mixture model fit in the original sample of cells, where estimates lower than 0.05 indicate a poor fit for the mixture model.

6.2 Bootstrap parameter estimates

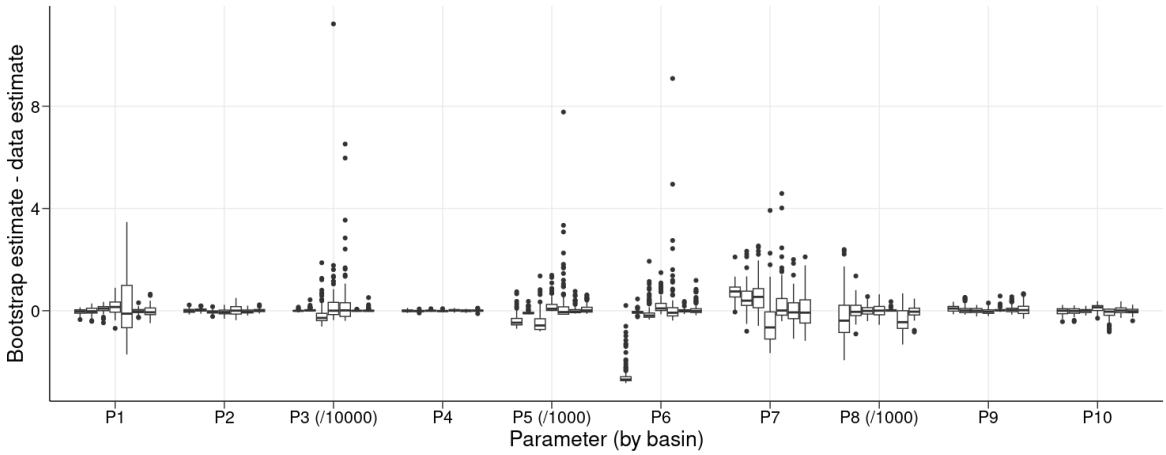

Figure 9: Boxplots of the bootstrapped parameter estimates for the spatial conditional extreme model fits minus the parameter estimates of the model fit to the full data set for each basin. Parameter estimates for each basin are plotted for each parameter in ascending order from basin 1 to basin 8.